Article

Gated CO$_2$ permeation across dynamic graphene pores

Luc Bondaz[1,3], Anshaj Ronghe [2,3], K. Ganapathy Ayappa [2] ✉ & Kumar Varoon Agrawal [1] ✉

Oxidation of graphene has been successfully used to incorporate semiquinone (C = O)-functionalized Å-scale pores, yielding attractive carbon capture performance. However, the true potential of such pores has remained unclear due to a lack of dedicated mechanistic studies. Herein, using molecular dynamics (MD) simulations, we show that C = O displays a strong molecular-interaction-dependent dynamic motion, leading to a distribution in the pore limiting diameter (PLD), comparable to the size differences between CO$_2$, O$_2$, and N$_2$. Dynamic open and closed pore states are observed in small pores, making impermeable pores CO$_2$-permeable. The strong molecular interaction eliminates effusive transport, resulting in selective gating of CO$_2$ from O$_2$ and N$_2$, even from large PLD pores which are expected to be nonselective. Finally, the transition-state-theory (TST) calculations validated against MD simulations reveal the immense potential of porous graphene for carbon capture beyond the state-of-the-art membranes. These insights will inspire improved graphene membrane design, pushing the carbon capture frontier.

High-performance membranes have immense potential to improve carbon capture efficiency[1,2] if they can be designed to yield a high CO$_2$ selectivity and a high CO$_2$ permeance[3]. Nanoporous atomically thin membranes (NATM), particularly porous graphene, have attracted substantial attention[4–9]. A single translocation event across the zero-dimensional pore determines selective transport[10–12]. Attractive gas separation performance has been observed[7,13–19], with selectivity arising from relative mass[8,20], molecular size[15,21–28], and binding affinity[16,19,29,30] differences. An accurate prediction of capture performance from graphene pores is needed to highlight the true potential of NATM. This will help design improved membranes for carbon capture.

Accurate and rapid computation of capture performance from realistic CO$_2$-selective pores, mimicking those formed in experiments, is needed. Å-scale pores in graphene for CO$_2$ separation are prepared by oxidation involving controlled lattice gasification[5,22,31–37]. The resulting pore edges are passivated with O functional groups[38–40]. These groups evolve from the chemisorption of a single epoxy followed by an organization of epoxies in a cluster (Supplementary Section S1)[37]. When the cluster size is sufficiently large, strain-mediated C-C bond cleavage followed by gasification yields a carbon vacancy defect (pore) with ether[41] and semiquinones (C = O) decorated at the pore edge[40,42–44]. Pores formed in this way have yielded attractive carbon capture performances, however, pores terminated with C = O have not been explored by computational studies.

Extensive computational studies have been conducted to analyze gas transport from graphene pores[10,45,46] since attractive gas separation from graphene pores was first predicted in the year 2009[4]. For simplicity, early studies probed pore edges devoid of functional groups and assumed rigid apertures with a fixed pore-limiting diameter[47–52]. Other studies probed pore edges passivated with atomic H, N, or O, however, gas transport was still investigated assuming a rigid aperture with a fixed pore limiting diameter (PLD)[4,49,53–58]. When lattice flexibility and vibrational dynamics were included, PLD modulation[59] and enlargement[60] were predicted, resulting in an increased gas permeance[11]. However, the pores decorated with the C = O group have not been studied and one expects the pore edge C = O group to interact favorably with molecules showing a quadrupole moment,

[1]Laboratory of Advanced Separations, Ecole Polytechnique Fédérale de Lausanne, Sion, Switzerland. [2]Department of Chemical Engineering, Indian Institute of Science, Bangalore, India. [3]These authors contributed equally: Luc Bondaz, Anshaj Ronghe. ✉e-mail: ayappa@iisc.ac.in; kumar.agrawal@epfl.ch

such as CO_2, and even flip-flop across the plane of the pore. This is expected to result in a unique occupancy-dependent guest environment, which could strongly control transport and the resulting separation performance. However, such guest-molecule-induced dynamics of $C=O$ have not been studied.

Small pores in graphene impose an energy barrier for the translocation of gas molecules. When the energy barrier becomes large, the transport event becomes a rare event in the MD simulations, which makes accurate measurement of gas separation performance challenging. Transition-state-theory (TST), which estimates the transport rate based on a classical energy barrier event, is particularly valuable in predicting transport rates and carbon capture performance in these cases. However, TST calculations have been mainly used to predict qualitative trends, and gas flux predicted by TST has not been validated, e.g., with predictions from MD simulations.

Herein, we report a unique transport behavior of gases in the presence of $C=O$ at the pore edge. $C=O$ bond exhibits a dynamic out-of-plane motion based on the extent of interaction with the gas molecule. The PLD, often assumed to be a constant, is found to have a large variance. Small pores with a strong molecular confinement exhibit a distinct open and closed state at a given temperature. The dynamic motion makes small pores CO_2 permeable, which would otherwise be impermeable with rigid PLD. The strong interaction of CO_2 with $C=O$ ensures adsorbed-phase transport even at elevated temperatures, resulting in a selective gating of CO_2 over O_2 and N_2 even from large pores, which would otherwise be nonselective. Finally, a quantitative agreement is achieved between the flux predicted by the TST calculations and the translocation rates from the MD simulations. This will allow one to avoid time-consuming and expensive simulations while overcoming the lack of statistics faced by rare translocation events. These insights highlight the high potential of porous graphene membranes for carbon capture and will inspire improved membrane design.

Results

Carbon capture from flue gas emission requires the separation of CO_2 from N_2 and O_2. CO_2/O_2 separation is more challenging than CO_2/N_2. O_2 permeates faster than N_2 because of its smaller kinetic diameter (3.30, 3.46, and 3.64 Å for CO_2, O_2, and N_2, respectively). However, studies on CO_2 transport across graphene pores primarily focus on CO_2/N_2 separations[18,49,55,61]. CO_2/O_2 separation has received much less attention. For several critical emissions, such as from natural gas combined cycle and cement plant, O_2 concentration in the flue gas can be as high as 10%, making this separation important[3]. Therefore, we focus on CO_2/O_2 separation. CO_2/N_2 separation was also studied, and results confirmed that CO_2/N_2 selectivities are much higher than those of CO_2/O_2.

MD simulation configuration

The MD simulation configuration used to analyze gas transport consists of graphene hosting 16 identical pores dividing feed and permeate chambers. The simulation box is enclosed in the z-direction by walls made of pristine graphene (Fig. 1a) with potentials similar to those used in the literature[41,44,62]. At the start of the simulation, the feed side has an equimolar CO_2/O_2 mixture while the permeate side is under vacuum.

Three Å-scale pores, pore-10, pore-13, and pore-16 are investigated. The digits represent the number of missing carbon atoms for forming pores (Fig. 1b–d). For a given number of missing carbon atoms, the pore skeleton is consistent with the most probable structure reported in the literature, validated by the observation under microscopy[15,63]. Pore edges are functionalized with $C=O$ (3–4 edge atoms) and ether groups (rest of the pore edge atoms). The assignment of the number of $C=O$ is consistent with the experimental data based on the concentration of $C=O$ per pore when pores are created by oxidation[44]. The remaining pore edge atoms are passivated by ether because, upon oxidation, ether is formed at the center of the oxygen
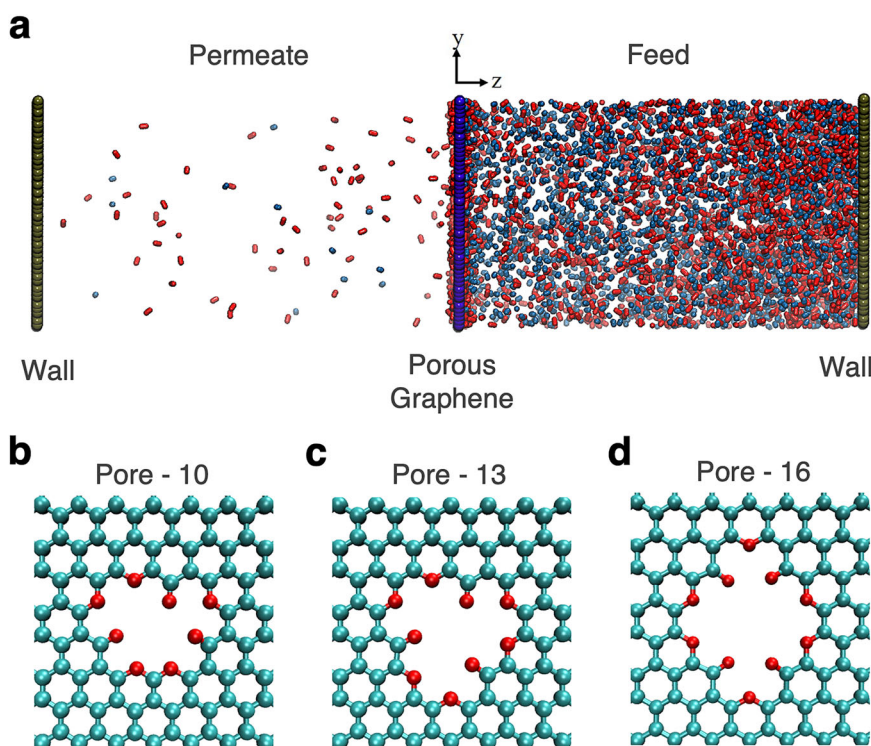
Fig. 1 | **MD simulation configuration used to examine the effectiveness of O-functionalized graphene pores for CO_2/O_2 separation. a** System details of the MD simulations with different components. **b**–**d** O-functionalized graphene pores in this study. Pore-10, pore-13, and pore-16 are prepared by removing 10, 13, and 16 carbon atoms, respectively, from the graphene lattice, followed by pore edge termination with ether and $C=O$. C and O atoms are represented in teal and red, respectively.
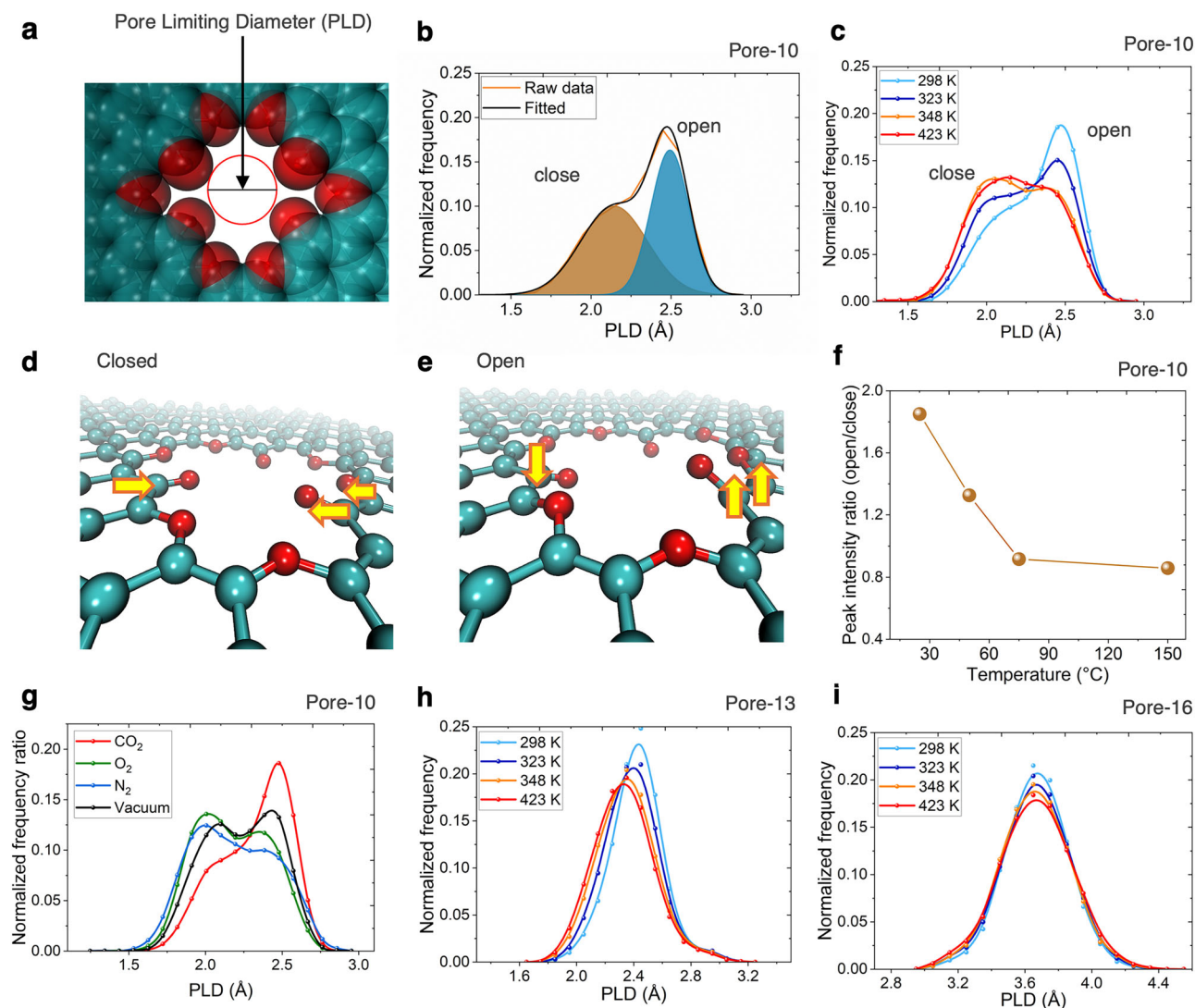
Fig. 2 | Pore limiting diameter (PLD) distribution for pore-10, pore-13, and pore-16 in the presence of CO_2/O_2 mixture as a function of temperature. a Illustration of the PLD – the largest van der Waals sphere that can be accommodated inside an oxygen-functionalized pore. C and O atoms are represented in teal and red, respectively. **b** PLD distribution of the pore-10 at 298 K with open and closed states depicted. **c** PLD distributions of pore-10 for various temperatures. **d**, **e** Illustration of the closed and open pores. Yellow arrows depict the atoms in and out of the plane. **f** The ratio of the peaks corresponding to the open and closed states for pore-10. **g** PLD distribution of the pore-10 at 298 K for different gas. PLD distribution of (**h**) the pore-13 and (**i**) the pore-16 as a function of temperatures. PLD distributions are based on a minimum of 15000 data points.

cluster[41]. The periodic arrangement of C = O bonds was confirmed by DFT calculations (Supplementary Section S2).

Dynamic gating of CO_2

The C = O group is observed to be dynamic, leading to modulation of the electron density gap in the pore. PLD, defined as the largest van der Waals sphere that can be accommodated inside the pore[56,64], (Fig. 2a) was evaluated every 50 ps at 298 K in the presence of the CO_2/O_2 feed. A distinct PLD distribution is observed for all three pores (Fig. 2b,h,i), indicating that the PLD is not a single value as often assumed. Strikingly, the corresponding variance (up to ~0.24 Å) is significant, considering that the difference in kinetic diameters of CO_2 and O_2 is only 0.16 Å.

At 298 K, pore-10 PLD has a distinct shoulder, indicating the presence of two states. One with a mean PLD of 2.4 Å and second with a mean PLD of 2.0 Å (Fig. 2b). Snapshots of the pore corresponding to these two states reveal that the larger PLD is manifested when C = O swings out-of-plane of the pore (open state), while the smaller PLD occurs when they are in-plane (closed state, Fig. 2d–e).

The relative occurrence of the open/closed state is analyzed by taking the ratio of the peak intensity of the two states (Fig. 2f). Pore-10 open state is found to be more probable than the closed state. The population of the open state decreases with increasing temperature (Fig. 2c, f). This can be explained by stronger interactions of CO_2 with C = O at lower temperatures, favoring an open state. To test this hypothesis further, pore-10 is exposed to pure CO_2, O_2, and N_2 gases and a vacuum (Fig. 2g). A distinct preference for the open state is established only in the case of CO_2. In contrast, a stronger preference for the closed state is observed for O_2 and N_2, which have weaker interactions with the pore.

For larger pores, the two distinct states were not observed (Fig. 2h,i). For pore-13, PLD decreases slightly from 2.45 to 2.35 Å when temperature is increased from 298 to 423 K, consistent with higher interaction with CO_2 at lower temperatures. The largest pore (pore-16) has a single peak at 3.65 Å, indicating that the confinement is not strong enough to alter the PLD (Fig. 2i). These observations confirm that a strong interaction between C = O and CO_2 results in the accommodation of CO_2 in the pore-10. This takes place via the out-of-
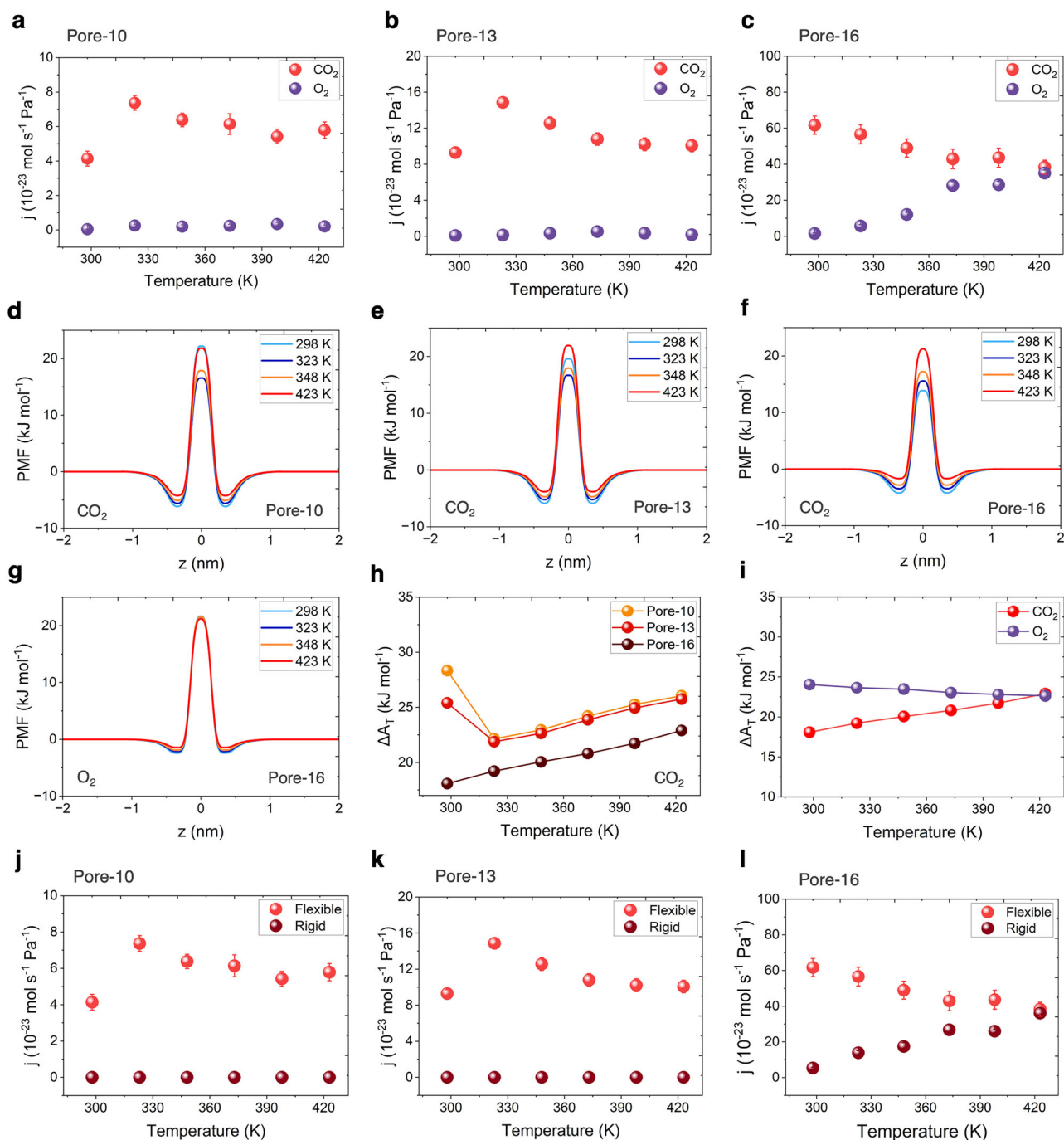
Fig. 3 | CO₂ and O₂ translocation across dynamic O-functionalized pores.
Translocation rates (**j**) of CO_2 and O_2 as a function of temperature through porous graphene hosting dynamic (**a**) pore-10, (**b**) pore-13, and (**c**) pore-16. Potential of mean force (PMF) profiles for the translocation of CO_2 molecules from (**d**) pore-10, (**e**) pore-13, (**f**) pore-16, and O_2 molecules from (**g**) pore-16. The porous graphene is located at z = 0, and the regions z > 0 and z < 0 depict the feed and permeate sides, respectively. The error bars represent the standard deviation in mean. Free energy barriers (ΔA_T) for the translocation of (**h**) CO_2 through pore-10, pore-13, and pore-16 and (**i**) CO_2 and O_2 through pore-16. Translocation rates of CO_2 as a function of temperature through porous graphene hosting dynamic and rigid (**j**) pore-10, (**k**) pore-13, and (**l**) pore-16. The error bars represent the standard deviation in mean.

plane motion of C = O. A single state is observed for pore-16 because CO_2 can be accommodated in the in-plane configuration. The above analysis reveals that C = O is dynamic and makes the pore environment dynamic. These observations from MD simulations are consistent with previous experimental work[22], where fluctuation of gas transport could be observed across 2D pores generated by oxidation.

The gas translocation rate, *j*, is evaluated from the cumulative number of molecules crossing the graphene pore as a function of time (Supplementary Section S3, Fig. 3a–c). An interesting trend concerning

temperature is observed. For smaller pores (pore-10 and pore-13), a two-fold increase in j_{CO2} occurs from 298 to 323 K. This can be explained by the strong interactions between CO_2 and oxygen functional group. At 298 K, CO_2 can remain in the pore for up to 3.5 ns, thereby preventing further translocation events (Supplementary fig. 8). The mean residence time of CO_2 is drastically reduced from 298 to 323 K: 30.6 and 17.3 ps for 298 and 323 K respectively, enabling higher translocation rates. Above 323 K, a steady decrease in translocation rate is observed for j_{CO2}. A key finding is negligible O_2

translocation for pore-10 and pore-13 in the 30 ns long simulations. These pores are highly selective to CO_2. Similar trends are observed at pore-16, where the pores are selective to CO_2 at lower temperatures; however, the O_2 translocation rate increases at higher temperatures. We reconcile these different trends in translocation rate by examining the free energy for translocation through the pores.

The potential of mean force (PMF) profiles for CO_2 translocation through all three pores were computed to understand the underlying energetics that determine transport (Fig. 3d–f). We quantify the free energy barrier for translocation (ΔA_T) by calculating the differences in PMFs at the center of the pore ($z = 0$) and the position where the minima in the PMFs are observed on the feed side (adsorbed state; see "Methods" section). We note that PMF computations in the literature are typically carried out for a single molecule translocating under vacuum conditions. In this study, PMF computations are carried out in the mixture to represent the free energy landscape under realistic mixture transport conditions. ΔA_T for CO_2 is the highest for the smallest pore (pore-10), decreasing as the pore size increases (Fig. 3h). Interestingly, ΔA_T values for pore-10 and pore-13 show a decrease when temperature increases from 298 to 323 K increasing monotonically for higher temperatures thereafter. For pore-16, where the confinement is the least, ΔA_T increases monotonically with temperature for CO_2; however, the opposite is observed for O_2, where a slight decrease occurs with increasing temperature (Fig. 2g, i).

The trend in j_{CO_2} correlates well with the decrease in ΔA_T from 298-323 K, and the steady decrease from 323-423 K is consistent with the increasing free energy barrier for translocation (Fig. 3a, b, h). The lower flux at 298 K is observed despite the larger pore size sampled (Fig. 2c). In addition to the higher free energy barrier at 298 K, CO_2 has a substantially higher residence time in the pore (3.5 ns), thereby preventing further translocation events (Supplementary fig. 8). The mean residence time of CO_2 is drastically reduced from 298 to 323 K: 30.6 and 17.3 ps for 298 and 323 K respectively, enabling higher translocation rates. The translocation trends for pore-16 follow the temperature dependence of free energy (Fig. 3c, i). O_2 has a larger kinetic diameter than CO_2. Given that CO_2 translocation follows an energy barrier, one expects O_2 to experience an even more significant barrier. This is indeed observed from the PMF calculation (Fig. 3i) translating into a slower translocation rate for O_2 than CO_2, leading to highly selective CO_2 transport.

Simulations with rigid pores were carried out to understand the impact of the dynamic motion of C = O on gas transport. In the rigid case, pore-10 and pore-13 were found to be impermeable (Fig. 3j–k). For pore-16, while the CO_2 permeation event is observed from the rigid pores, the translocation rate is underestimated by an order of magnitude (Fig. 3l). This observation is consistent with previous reports in the literature[60]. A similar flux underestimation was observed for the CO_2/N_2 case (Supplementary fig. 6–7). This demonstrates that neglecting functional group dynamics for graphene pores leads to erroneous results, making highly permeable and selective pores impermeable to CO_2.

Competitive uptake of CO_2

The dynamics of the flexible pore functional group leading to dynamic PLD must be associated with a competitive uptake of CO_2; otherwise, the selective gating of CO_2 discussed above would not be feasible. To understand this, the 1D density distributions of CO_2 and O_2 on the porous graphene lattice (pore-13) were analyzed (Fig. 4a–b). It shows that CO_2 adsorbs much more strongly than O_2 in the entire temperature range (298-423 K). At 298 K, the CO_2 population is 8-fold higher than that of O_2 in the feed side of the pore, and a weak density peak on the permeate side is observed only for CO_2. This competitive uptake is due to strong charge polarity in the C = O group, which attracts CO_2 to electronegative O. As expected, the interaction weakens at higher temperatures, reducing the CO_2/O_2 occupancy ratio to 2.5 at 423 K. Similar trends are observed for pore-10 and pore-16 (Supplementary figs. 9 and 10).

Although 1D density profiles are highly informative, yet it does not pinpoint whether gas molecules tend to adsorb onto the lattice and/or oxygen functionalized pores. In that regard, the 2D density profiles provide crucial insights into the distribution of gases on the lattice near and away from the pore. The carbon lattice of the graphene, not containing the pore, is referred to as the surface region. CO_2 populates the pore region to a significantly greater extent than the surface region (Fig. 4c–d). At 298 K, the CO_2 population in the pore region is ~1.9–2.5 times greater than the surface region. At 423 K, the overall CO_2 population decreases. Nevertheless, relatively higher adsorption on the pore is still observed compared to the lattice (Fig. 4d). In contrast, a negligible population of O_2 is observed in the pore region (Fig. 4e, f). O_2 adsorbs predominantly on the graphene lattice away from the pore. We infer that the high propensity of CO_2 towards the pore region inhibits O_2, contributing to the selective CO_2 translocation. Similar observations have been made in crown-ether pores[18]. However, pore dynamics and gating are not at play in these pores. Therefore, competitive adsorption of CO_2 near the C = O group plays a crucial role in pore dynamics and selective gating.

An adsorption peak in the density profiles is also observed on the permeate side (Fig. 4a, b). This agrees well with the literature on transport dominated by surface or adsorbed-phase transport[47,65]. In this case, after translocating through the pores, gases tend to first adsorb on the permeate side of graphene, and the final permeation event takes place when the gas desorbs from this adsorbed layer (Fig. 5a, i, and Supplementary fig. 11). PMF calculations confirm this, where a free energy valley on the permeate side was also observed (Fig. 3d–g).

A competing transport mode to the surface transport is direct transport, where a gas molecule impinges on the pores directly from the gas phase (Fig. 5a, ii)[47]. For small pores, there is no consensus in the literature on the extent of direct versus surface transport. It is convenient to model CO_2 transport by assuming direct transport, where the transport rate can be calculated by adding an energy barrier term to the effusive transport rates (modified effusion model)[5,47,58,59]. We show that CO_2 primarily transports via the surface transport mechanism. For this, the contribution of direct and surface flux to the overall transport rate is quantified. Tracking the path of CO_2 in the MD simulation, we find that surface flux overwhelmingly dominates CO_2 transport, with 99% of translocation events taking place by surface pathway at room temperature. Even at elevated temperatures (e.g., 423 K), surface flux contributes 90% of the total translocation events. Interestingly, the surface flux pathway is also dominant for O_2, a gas with a relatively weak interaction with the pore (67% and 55% at 298 and 423 K, respectively). The dominance of surface flux and the competitive adsorption of CO_2 has an important ramification, i.e., selectivity can be achieved from pores with pore size larger than the size of the molecule, as observed in this study for pore-16.

Flux Prediction by Transition State Theory

TST-based calculation of gas flux through a zero-dimensional pore is promising for predicting the gas separation performance for NATM. It helps one bypass lengthy MD simulations, especially when molecular transport is a rare event, e.g., for O_2 in the current study[11,66]. While TST calculations have been used in the past to estimate transport rates, the propagation for error is high mainly because of assumptions made for the estimation of energy barrier and pre-exponential coefficient. As a result, gas separation performance from TST calculation has not been validated by MD simulation. Herein, we evaluate the potential for using TST to predict the translocation rates and pore selectivities. Using TST[11], the translocation coefficient (k_{trans}^{TST}) is calculated using,

$$k_{trans}^{TST} = A_{trans}^{TST} \exp\left(\frac{-\Delta E}{RT}\right) \qquad (1)$$
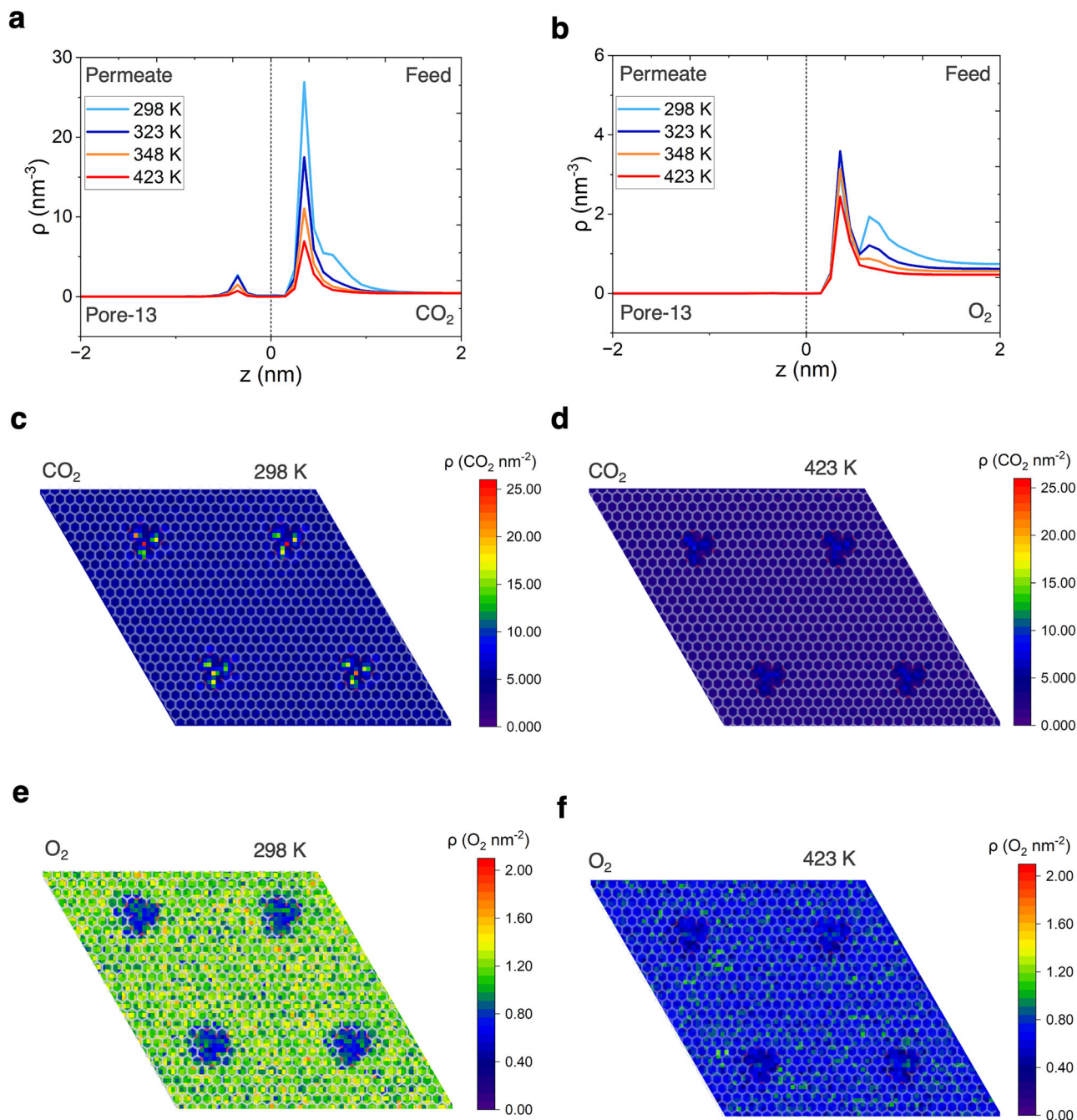
Fig. 4 | Density distributions of CO₂ and O₂ on graphene lattice hosting pore-13 as a function of temperature. a, **b** Number densities (ρ) of CO_2 and O_2 molecules near the porous graphene positioned at $z = 0$. Surface density profiles of (**c**, **d**) CO_2 and (**e**, **f**) O_2 within 1 nm on the feed side at 298 (**c**, **e**) and 423 K (**d**, **f**). Note that the limits for the color bars are different for CO_2 and O_2.

where A_{trans}^{TST} is the translocation prefactor, which can be expressed as,

$$A_{trans}^{TST} = \frac{1}{2L} |\dot{z}(0)| \exp\left(\frac{\Delta S}{R}\right) \quad (2)$$

where L is the half-peak width of the probability distribution of gases along the translocation trajectory function[11], which is 0.18 nm and 0.27 nm for CO_2 and O_2, respectively. R is the universal gas constant. ΔS and ΔE are the entropic and energy barriers associated with the translocation of a gas molecule through the pore. The values of ΔS and ΔE are obtained by using a linear fit to the ΔA_T versus T data (Supplementary figs. 12, 13 and Supplementary Table 1). $|\dot{z}(0)|$ is the most probable velocity when a molecule crosses the barrier at $z = 0$.

Within, TST $|\dot{z}(0)|$ is approximated using the Maxwell–Boltzmann distribution:

$$|\dot{z}(0)| = \sqrt{\frac{2k_B T}{\pi m}} \quad (3)$$

where k_B and m are the Boltzmann constant and mass of a single molecule, respectively. From Eqs. 1–3, the translocation rate is then computed using:

$$j^{TST} = \frac{k_{trans}^{TST}[CO_x]A_{pore}}{P} \quad (4)$$

a
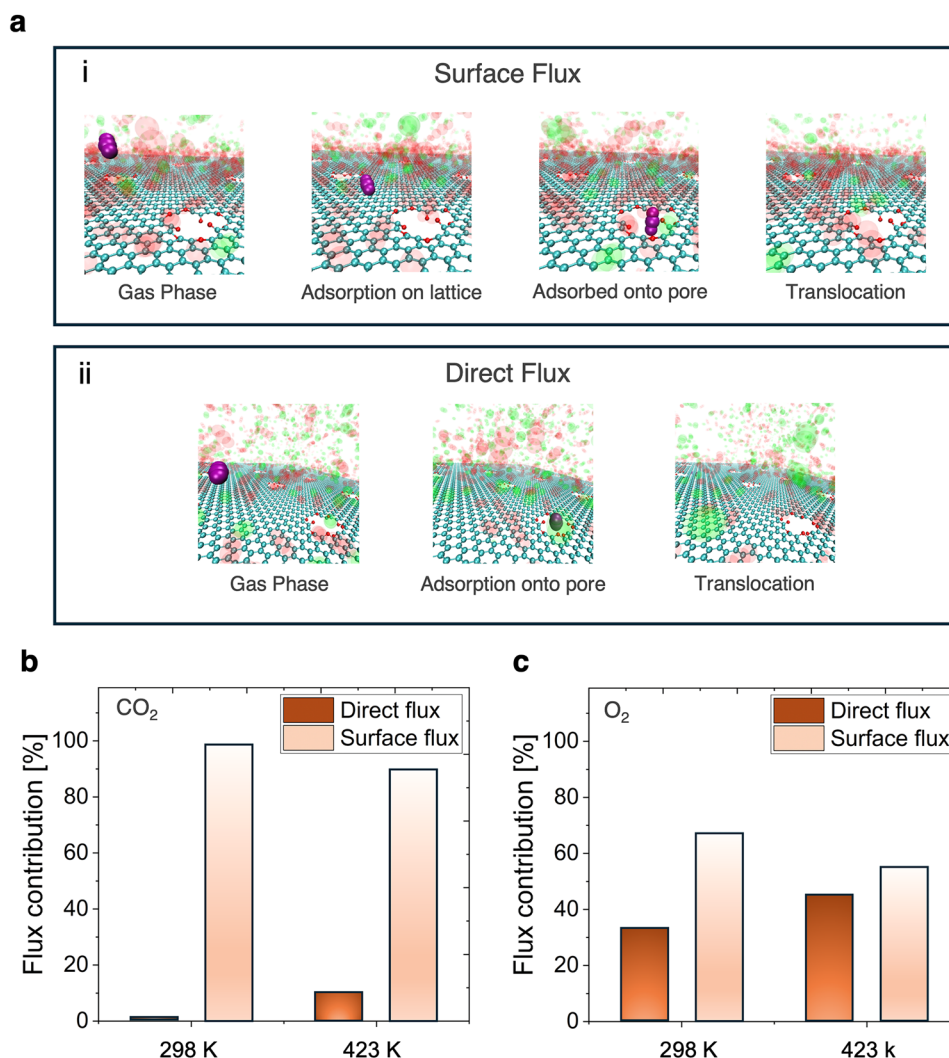
Fig. 5 | Analysis of surface and direct flux for CO₂ and O₂ across O-functionalized graphene pores. a Snapshots demonstrating (i) surface and (ii) direct flux across a porous graphene lattice. Contribution of the surface and direct fluxes towards transport of (**b**) CO₂ and (**c**) O₂ across pore-13 at 298 and 423 K.

where $[CO_x]$ is the concentration of gas molecules adsorbing onto the pore, P is the pressure on the feed side, and A_{pore} is the pore area (Supplementary Tables 2-5). Based on Eq. 4, TST significantly underpredicts the gas translocation rate (Fig. 6d). To understand the reason for this underestimation, we compared ΔE and A_{trans}^{TST} computed from MD simulations and TST (Fig. 6b, c, and Supplementary Section S9). ΔE is similar for both TST and MD and thus, is not responsible for TST underpredictions. This confirms the negligible occurrence of recrossing during the MD simulations[11]. A_{trans}^{TST} is found to be significantly lower than A_{trans}^{MD} explaining underestimation of gas flux by TST. This can be explained by approximation of $|\dot{z}(0)|$ using the Maxwell−Boltzmann distribution, where particles are considered free from interactions with the pore. However, in confined pores, molecules experience a strong interaction. This is especially important for C = O terminated pores, as in this study. In order to account for interactions with the pore, we introduce the velocity, v_c which is computed based on free energy barriers, ΔA_T (Fig. 3h, i) as follows[54]:

$$\frac{1}{2} M v_c^2 = \Delta A_T \tag{5}$$

where M is the molar mass of the molecule. We use the following expression for translocation prefactor in Eq. 2:

$$A_{trans}^{TST}\big|_{corrected} = \frac{1}{2L} v_c \exp\left(\frac{\Delta S}{R}\right) \tag{6}$$

$A_{trans}^{TST}\big|_{corrected}$ is in very good agreement with A_{trans}^{MD}, demonstrating the accuracy of the correction factor (Fig. 6c). Moreover, the prediction of the translocation rates of gases is significantly improved using the velocity based on the free energy barrier (Fig. 6e). Additionally, good agreement in the pore selectivities derived from MD and TST is observed (Fig. 6f). Here, mixture selectivity, S, is the ratio of gas translocation rates (Eq. 7).

$$S = \left(\frac{j_{CO_2}}{j_{O_2}}\right) \tag{7}$$

These calculations show that graphene pores are highly attractive for carbon capture. j_{O2} is low for pore-10 and pore-13. However, we can confidently say that S is larger than 100 for these pores. To bypass the lack of statistics faced by O₂ translocation across small pores, corrected transition state can be used (Supplementary Section S10). Given that ΔA_T
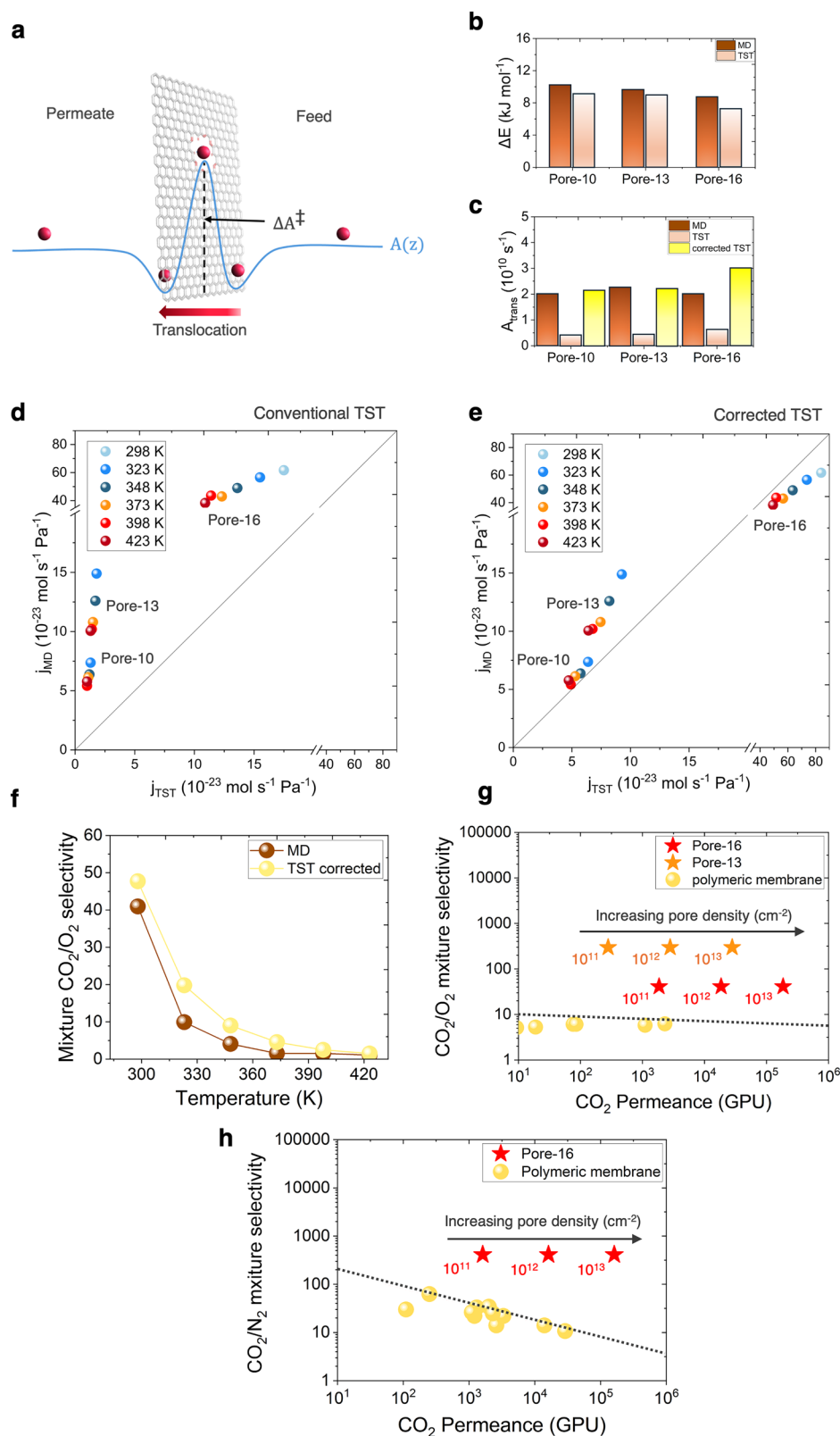
Fig. 6 | Transition state theory for predicting CO_2 translocation across 2D graphene pores. a Schematic of the transition state theory of a gas translocating across graphene pores. $\triangle A^{\ddagger}$ is the free energy of pore translocation. **b** Comparison of energy barrier (ΔE) estimated using MD and TST for CO_2 translocation through different pores (c) Comparison of translocation prefactor (A_{trans}) estimated using MD, TST (323 K) and corrected TST predictions (323 K) for CO_2 translocation through different pores. (**d**) Comparison of the translocation rates obtained from MD simulations and TST calculations for CO_2 translocating through different pores. (**e**) Comparison of the translocation rates obtained from MD simulations and corrected TST calculations for CO_2 translocating through different pores. (**f**) Comparison of CO_2/O_2 mixture selectivity obtained from MD simulation and corrected TST calculations for pore-16. (**g**) CO_2/O_2 mixture selectivity and CO_2 permeance for state-of-art polymeric membranes and graphene pores as a function pore density. (**h**) CO_2/N_2 mixture selectivity and CO_2 permeance for state-of-art polymeric membranes and graphene pore-16 as a function pore density. Robeson upper bond is represented for a selective layer of 1 micrometer in panels g and h (dashed line)[82].

steadily decreases with temperature[42] from 298 to 423 K, O_2 translocation rate at 298 K for both pore-10 and pore-13 can be reliably predicted. Interestingly, both pores demonstrate very high CO_2/O_2 selectivity at room temperature: 196 and 297 for pore-10 and pore-13 respectively. For pore-16, S ranges from 42 and 10 at 298 and 323 K, respectively, dropping to 1 at 423 K.

Additionally, to understand the application of pore-16 in carbon capture, CO_2/N_2 selectivity was also studied. CO_2/N_2 selectivity is expected to be higher than CO_2/O_2, given that N_2 is larger than O_2. Indeed, pore-16 yielded very attractive CO_2/N_2 mixture selectivities, exceeding 400 at 298 K (Supplementary fig. 6). This shows that pore-16, considered too large for selective CO_2 permeation, is attractive for rapid and selective transport of CO_2. Pore-13 is expected to yield very high CO_2/N_2 selectivity, given the very high barrier faced by N_2 upon PMF calculations to translocate through pore-13. Porous graphene membrane hosting C = O functionalized 2D pores outperforms state-of-the-art membranes (Fig. 6g, h). In particular, a density $\geq 10^{11}$ pores cm^{-2}, feasible in pore generation by oxidation, yields a very attractive CO_2 permeance (up to 10000 gas permeation units or GPU, 1 GPU = 3.35×10^{-10} mol m^{-2} s^{-1} Pa^{-1}) accompanying large CO_2/O_2 and CO_2/N_2 selectivities. Such high performance is expected to reduce the energy input and cost of carbon capture, even from dilute point source emissions[1–3].

Graphene pores generated via oxidation have demonstrated high stability for gas separation[15–19]. C = O group is thermally stable[40]. Recent studies have shown the feasibility of scaling up porous graphene membranes for carbon capture to an area of 50 cm^2[67]. However, a considerable gap remains between simulations and experimental results. This discrepancy can be attributed to two key factors. First, simulation studies focus on a few pores, whereas porous graphene membranes have a pore size distribution (PSD). Second, the process of fabricating porous graphene membrane introduces pinhole defects, which negatively impact the membrane's overall separation performance. To bridge this gap, we predicted gas transport from an ensemble of pores with PSD (Supplementary Section S11). By comparing the experimentally observed permeance with our predicted values, we estimated the coverage of pinhole defects to be ~37.6 μm^2 per m^2. A crucial strategy for maximizing the gas separation performance of porous graphene membranes is to minimize these pinhole defects. Our findings suggest that reducing pinhole defects by 90% could lead to a fivefold increase in CO_2/O_2 selectivity (Supplementary fig. 20).

We report that Å-scale graphene pores decorated with C = O groups, generated from the oxidation of graphene, selectively gate CO_2 largely driven by the dynamic behavior of pore edge C = O. The gas permeance and selectivity predicted from graphene pores are shown to be highly erroneous with the assumption of fixed PLD, indicating that fixed PLD calculation should be only considered for the cases with negligible molecule-pore interactions. Strong interactions between the pore edge functional group (C = O) with gas molecules control transport. These interactions open a seemingly impermeable pore or provides high selectivity from a seemingly nonselective pore. Therefore, capturing these interactions is essential for reliable gas flux and permeance predictions. TST-based rate calculation can be used to accurately predict gas flux and corresponding selectivity if the assumptions in the TST formulation are corrected to account for pore confinement effects. This allows one to rapidly predict gas permeance events even when the energy barrier for pore translocation is high, a scenario that greatly limits the applicability of MD simulations. These findings pave the way to understand and predict mass transport in realistic graphene pores and will guide the design of graphene membranes for molecular separation.

Methods

Density functional theory calculations

Quantum ESPRESSO package was used for performing density functional theory calculations[68,69] to obtain the relaxed structures of oxygen-functionalized pores. The plane-wave basis sets were employed to carry out the electronic wave function expansion with the cutoffs of 50 Ry and 500 Ry employed for the wave function and charge density, respectively. Perdew-Bruke-Ernzerhof functional[70] was used to describe the exchange-correlation, and ultrasoft pseudopotentials[71] were utilized to model the interactions between the ionic core and valence electrons. A vacuum of 2.0 nm was incorporated along the direction normal to the oxygen-functionalized pores' surface to avoid interactions between the periodic images. Owing to the large supercell, the Brillouin zone sampling was restricted to the Γ point, and the Broyden-Fletcher-Goldfar-Shanno scheme was employed to perform structural relaxation until the Hellmann-Feynman forces were less than 10^{-3} Ry $Bohr^{-1}$. London dispersion corrections were described using DFT-D2 functional[72]. Finally, the relaxed unit cells were replicated in the x-y plane to generate the porous graphene hosting 16 oxygen-functionalized pores[44].

Molecular dynamics simulations

Molecular dynamics simulations to examine the effectiveness of oxygen-functionalized graphene pores for CO_2/O_2 separation were performed using GROMACS 5.1.4 simulation package[73,74]. An equimolar mixture of CO_2/O_2 containing 2500 molecules of each species was initially equilibrated at the temperatures of 298, 323, 348, 373, 398, and 423 K and pressure of 50 bar for each temperature, in a canonical ensemble. This resulted in 6 equilibrated simulation boxes, and the volumes of these boxes are given in Supplementary Table 13, which were determined from the open-source program CoolProp[75]. Subsequently, to generate the feed side of the gas mixture, the equilibrated simulation boxes were enclosed along the z direction by the porous graphene hosting 16 oxygen-functionalized pores and a reflective wall made of a single-layer pristine graphene sheet. In order to generate the permeate side, another reflective wall was used such that the volume of the permeate side is the same as that of the reservoir. A similar simulation protocol has been employed previously to study gas separation[41] and water evaporation[44,62] from graphene nanopores. Owing to the hexagonal graphene lattice, a parallelepiped simulation box was used with a cross-sectional area of 142.18 nm^2.

During the course of the simulation, all atoms of the graphene except the oxygen functional groups terminating the pores were fixed in their respective atomic positions. This was done to decouple the transport behavior of gases through oxygen functionalized pores from mechanical deformation phenomena. The oxygen functional groups were allowed both in-plane and out-of-plane motion with bond stretch and bond angle potentials in the force-fields to allow dynamic interactions with the gas molecules[41,44]. The Lennard-Jones interaction parameters and charges of the CO_2 and O_2 gas molecules were parameterized using the TraPPE model (Supplementary Table 14-15)[11,59,76]. On the other hand, all-atom optimized potentials for liquid simulation parameters were used for N_2 (Supplementary Table 16)[18,41] and functional groups terminating graphene pores[41,44,62,77]. Parameters developed by Cheng and Steele, were used to simulate the pristine lattice[11,78]. van der Waals interactions were modeled using Lennard–Jones potential with a cutoff of 1.2 nm, and Lorentz-Berthelot mixing rules were applied for the cross-interaction parameters for the Lennard-Jones potential between other unlike pairs. Additionally, the Particle Mesh Ewald algorithm was used to compute the long-range electrostatic interactions with a cutoff of 1.2 nm for real space force calculations. All the simulations were performed in a canonical (NVT) ensemble, and the temperature was controlled using the v-rescale thermostat with a time constant of 0.2 ps[11,41]. Each simulation was carried out for 30.5 ns with a time step of 1 fs, of which the first 2 ns were treated as the equilibration stage. In order to get better statistics, 3 simulation repeats of each system were performed, each with a varied initial configuration of gas molecules.

Potential of mean force calculations

The umbrella sampling method is used to evaluate the potential of mean force (PMF) profiles for gas permeation through the oxygen-functionalized graphene pores at different temperatures[79,80]. Force constants of 500–1000 kJ mol^{-1} nm^{-2} are used in the harmonic umbrella potential, and the z-coordinate of the probe gas molecule is varied from 2.0 to -2.0 nm in decrements of 0.05 nm, with the porous graphene located at $z = 0$. The probe gas molecule is free to move in the x-y plane bounded by the cylindrical region across the nanopore. This cylindrical region extends up to 2.0 nm into both the feed and permeate side of the nanoporous graphene and exhibits a diameter equal to the PLD of a given pore, and its center is the center of the PLD (as determined in Fig. 2). This resulted in 81 windows along the z direction, and each window is sampled for at least 15 ns, where the first 1.0 ns is treated as the equilibration stage. The collected data is analyzed using a weighted histogram analysis method[81].

Data availability

The authors declare that all the data supporting the findings of this study are available within the article and its Supplementary Information file. Source data are provided with this paper.

References

1. Merkel, T. C., Lin, H., Wei, X. & Baker, R. Power plant post-combustion carbon dioxide capture: An opportunity for membranes. *J. Memb. Sci.* **359**, 126–139 (2010).
2. Han, Y. & Ho, W. S. W. Polymeric membranes for CO$_2$ separation and capture. *J. Memb. Sci.* **628**, 119244 (2021).
3. Micari, M., Dakhchoune, M. & Agrawal, K. V. Techno-economic assessment of postcombustion carbon capture using high-performance nanoporous single-layer graphene membranes. *J. Memb. Sci.* **624**, 119103 (2021).
4. Jiang, D., Cooper, V. R. & Dai, S. Porous graphene as the ultimate membrane for gas separation. *Nano Lett.* **9**, 4019–4024 (2009).
5. Koenig, S. P., Wang, L., Pellegrino, J. & Bunch, J. S. Selective molecular sieving through porous graphene. *Nat. Nanotechnol.* **7**, 728–732 (2012).
6. Li, H. et al. Ultrathin, molecular-sieving graphene oxide membranes for selective hydrogen separation. *Science* **342**, 95–98 (2013).
7. Kim, H. W. et al. Selective gas transport through few-layered graphene and graphene oxide membranes. *Science* **342**, 91–95 (2013).
8. Celebi, K. et al. Ultimate permeation across atomically thin porous graphene. *Science* **344**, 289–292 (2014).
9. Mi, B. Scaling up nanoporous graphene membranes. *Science* **364**, 1033–1034 (2019).
10. Wang, L. et al. Fundamental transport mechanisms, fabrication and potential applications of nanoporous atomically thin membranes. *Nat. Nanotechnol.* **12**, 509–522 (2017).
11. Yuan, Z. et al. Mechanism and Prediction of gas permeation through sub-nanometer graphene pores: comparison of theory and simulation. *ACS Nano* **11**, 7974–7987 (2017).
12. Kidambi, P. R., Chaturvedi, P. & Moehring, N. K. Subatomic species transport through atomically thin membranes: present and future applications. *Science* **374**, eabd7687 (2021).
13. Tian, Z., Mahurin, S. M., Dai, S. & Jiang, D. Ion-gated gas separation through porous graphene. *Nano Lett.* **17**, 1802–1807 (2017).
14. Guo, W., Mahurin, S. M., Unocic, R. R., Luo, H. & Dai, S. Broadening the gas separation utility of monolayer nanoporous graphene membranes by an ionic liquid gating. *Nano Lett.* **20**, 7995–8000 (2020).
15. Huang, S. et al. Millisecond lattice gasification for high-density CO$_2$- and O$_2$-sieving nanopores in single-layer graphene. *Sci. Adv.* **7**, 1–12 (2021).
16. Ashirov, T. & Coskun, A. Ultrahigh permeance metal coated porous graphene membranes with tunable gas selectivities. *Chem* **7**, 2385–2394 (2021).
17. Hsu, K. J. et al. Multipulsed millisecond ozone gasification for predictable tuning of nucleation and nucleation-decoupled nanopore expansion in graphene for carbon capture. *ACS Nano* **15**, 13230–13239 (2021).
18. Luan, B. et al. Crown nanopores in graphene for CO$_2$ capture and filtration. *ACS Nano* **16**, 6274–6281 (2022).
19. Hsu, K. J. et al. Graphene membranes with pyridinic nitrogen at pore edges for high-performance CO2 capture. *Nat. Energy* **9**, 964–974 (2024).
20. Buchheim, J., Schlichting, K. P., Wyss, R. M. & Park, H. G. Assessing the thickness-permeation paradigm in nanoporous membranes. *ACS Nano* **13**, 134–142 (2019).
21. Suk, M. E. & Aluru, N. R. Ion transport in sub-5-nm graphene nanopores. *J. Chem. Phys.* **140**, 084707 (2014).
22. Wang, L. et al. Molecular valves for controlling gas phase transport made from discrete ångström-sized pores in graphene. *Nat. Nanotechnol.* **10**, 785–790 (2015).
23. Lin, L. C. & Grossman, J. C. Atomistic understandings of reduced graphene oxide as an ultrathin-film nanoporous membrane for separations. *Nat. Commun.* **6**, 8335 (2015).
24. Kidambi, P. R. et al. Nanoporous atomically thin graphene membranes for desalting and dialysis applications. *Adv. Mater.* **29**, 1700277 (2017).
25. Lu, Y. et al. Monolayer graphene membranes for molecular separation in high-temperature harsh organic solvents. *Proc. Natl. Acad. Sci.* **118**, e2111360118 (2021).
26. Shen, L. et al. Highly porous nanofiber-supported monolayer graphene membranes for ultrafast organic solvent nanofiltration. *Sci. Adv.* **7**, 1–10 (2021).
27. Cheng, C., Iyengar, S. A. & Karnik, R. Molecular size-dependent subcontinuum solvent permeation and ultrafast nanofiltration across nanoporous graphene membranes. *Nat. Nanotechnol.* **16**, 989–995 (2021).
28. Wang, J. et al. Cascaded compression of size distribution of nanopores in monolayer graphene. *Nature* **623**, 956–963 (2023).
29. Lee, J. & Aluru, N. R. Water-solubility-driven separation of gases using graphene membrane. *J. Memb. Sci.* **428**, 546–553 (2013).
30. Cohen-Tanugi, D. & Grossman, J. C. Water desalination across nanoporous graphene. *Nano Lett.* **12**, 3602–3608 (2012).
31. O'Hern, S. C. et al. Selective ionic transport through tunable sub-nanometer pores in single-layer graphene membranes. *Nano Lett.* **14**, 1234–1241 (2014).
32. Surwade, S. P. et al. Water desalination using nanoporous single-layer graphene. *Nat. Nanotechnol.* **10**, 459–464 (2015).
33. Yuan, Z., Benck, J. D., Eatmon, Y., Blankschtein, D. & Strano, M. S. Stable, temperature-dependent gas mixture permeation and separation through suspended nanoporous single-layer graphene membranes. *Nano Lett.* **18**, 5057–5069 (2018).
34. Yang, Y. et al. Large-area graphene-nanomesh/carbon-nanotube hybrid membranes for ionic and molecular nanofiltration. *Science* **364**, 1057–1062 (2019).
35. Sun, P. Z. et al. Exponentially selective molecular sieving through angstrom pores. *Nat. Commun.* **12**, 7170 (2021).
36. Cheng, P. et al. Differences in water and vapor transport through angstrom-scale pores in atomically thin membranes. *Nat. Commun.* **13**, 1–12 (2022).
37. Huang, S. et al. In situ nucleation-decoupled and site-specific incorporation of Å-scale pores in graphene via epoxidation. *Adv. Mater.* **34**, 2206627 (2022).
38. Yamada, Y. et al. Subnanometer vacancy defects introduced on graphene by oxygen gas. *J. Am. Chem. Soc.* **136**, 2232–2235 (2014).

39. Raffone, F., Savazzi, F. & Cicero, G. Controlled pore generation in single-layer graphene oxide for membrane desalination. *J. Phys. Chem. Lett.* **10**, 7492–7497 (2019).

40. Li, S. et al. Structure evolution of graphitic surface upon oxidation: insights by scanning tunneling microscopy. *JACS Au* **2**, 723–730 (2022).

41. Bondaz, L. et al. Selective photonic gasification of strained oxygen clusters on graphene for tuning pore size in the Å regime. *JACS Au* **3**, 2844–2854 (2023).

42. Larciprete, R. et al. Dual path mechanism in the thermal reduction of graphene oxide. *J. Am. Chem. Soc.* **133**, 17315–17321 (2011).

43. Sun, T. & Fabris, S. Mechanisms for oxidative unzipping and cutting of graphene. *Nano Lett.* **12**, 17–21 (2012).

44. Lee, W. C. et al. Enhanced Water Evaporation from Å-Scale Graphene Nanopores. *ACS Nano* **16**, 15382–15396 (2022).

45. Yuan, Z. et al. Gas Separations using nanoporous atomically thin membranes: recent theoretical, simulation, and experimental advances. *Adv. Mater.* **34**, 2201472 (2022).

46. Villalobos, L. F., Babu, D. J., Hsu, K. J., Van Goethem, C. & Agrawal, K. V. Gas separation membranes with atom-thick nanopores: the potential of nanoporous single-layer graphene. *Acc. Mater. Res.* **3**, 1073–1087 (2022).

47. Sun, C. et al. Mechanisms of molecular permeation through nanoporous graphene membranes. *Langmuir* **30**, 675–682 (2014).

48. Drahushuk, L. W. & Strano, M. S. Mechanisms of gas permeation through single layer graphene membranes. *Langmuir* **28**, 16671–16678 (2012).

49. Wu, T. et al. Fluorine-modified porous graphene as membrane for CO2/N 2 separation: Molecular dynamic and first-principles simulations. *J. Phys. Chem. C.* **118**, 7369–7376 (2014).

50. Shan, M. et al. Influence of chemical functionalization on the CO2/N2 separation performance of porous graphene membranes. *Nanoscale* **4**, 5477–5482 (2012).

51. Raghavan, B. & Gupta, T. H2/CH4 gas separation by variation in pore geometry of nanoporous graphene. *J. Phys. Chem. C.* **121**, 1904–1909 (2017).

52. Du, H. et al. Separation of hydrogen and nitrogen gases with porous graphene membrane. *J. Phys. Chem. C.* **115**, 23261–23266 (2011).

53. Xu, R. et al. High-performance carbon molecular sieve membrane for C2H4/C2H6 separation: molecular insight into the structure-property relationships. *Carbon* **201**, 24–36 (2023).

54. Liu, H., Dai, S. & Jiang, D. E. Insights into CO_2/N2 separation through nanoporous graphene from molecular dynamics. *Nanoscale* **5**, 9984–9987 (2013).

55. Liu, H., Chen, Z., Dai, S. & Jiang, D. E. Selectivity trend of gas separation through nanoporous graphene. *J. Solid State Chem.* **224**, 2–6 (2015).

56. Bondaz, L., Chow, C. M. & Karnik, R. Rapid screening of nanopore candidates in nanoporous single-layer graphene for selective separations using molecular visualization and interatomic potentials. *J. Chem. Phys.* **154**, 184111 (2021).

57. Tao, Y. et al. Tunable hydrogen separation in porous graphene membrane: First-principle and molecular dynamic simulation. *ACS Appl. Mater. Interfaces* **6**, 8048–8058 (2014).

58. Guo, J., Galliero, G. & Vermorel, R. From molecular sieving to gas effusion through nanoporous 2D graphenes: comparison between analytical predictions and molecular simulations. *J. Chem. Phys.* **159**, 084701 (2023).

59. Vallejos-Burgos, F., Coudert, F. X. & Kaneko, K. Air separation with graphene mediated by nanowindow-rim concerted motion. *Nat. Commun.* **9**, 1812 (2018).

60. Guo, J., Galliero, G. & Vermorel, R. How membrane flexibility impacts permeation and separation of gas through nanoporous graphenes. *Nano Lett.* **24**, 12292–12298 (2024).

61. Liu, H., Dai, S. & Jiang, D. E. Permeance of H2 through porous graphene from molecular dynamics. *Solid State Commun.* **175–176**, 101–105 (2013).

62. Ronghe, A. & Ayappa, K. G. Graphene nanopores enhance water evaporation from salt solutions: exploring the effects of ions and concentration. *Langmuir* **39**, 8787–8800 (2023).

63. Govind Rajan, A. et al. Addressing the isomer cataloguing problem for nanopores in two-dimensional materials. *Nat. Mater.* **18**, 129–135 (2019).

64. Kocaman, C., Bondaz, L., Rezaei, M., Hao, J. & Agrawal, K. V. Direct synthesis of nanocrystalline single-layer porous graphene for hydrogen sieving. *Carbon* **221**, 118866 (2024).

65. Yuan, Z., Misra, R. P., Rajan, A. G., Strano, M. S. & Blankschtein, D. Analytical prediction of gas permeation through graphene nanopores of varying sizes: Understanding transitions across multiple transport regimes. *ACS Nano* **13**, 11825–11833 (2019).

66. Vahdat, M. T. et al. Efficient Kr/Xe separation from triangular g-C3N4nanopores, a simulation study. *J. Mater. Chem. A* **8**, 17747–17755 (2020).

67. Hao, J. et al. Scalable synthesis of CO_2-selective porous single-layer graphene membranes. *Nat. Chem. Eng.* **2**, 1–22 (1950).

68. Giannozzi, P. et al. QUANTUM ESPRESSO: a modular and open-source software project for quantum simulations of materials. *J. Phys. Condens. Matter* **21**, 395502 (2009).

69. Hohenberg, P. & Kohn, W. Inhomogeneous electron gas. *Phys. Rev.* **136**, B864 (1964).

70. Perdew, J. P., Burke, K. & Ernzerhof, M. Generalized gradient approximation made simple. *Phys. Rev. Lett.* **77**, 3865–3868 (1996).

71. Vanderbilt, D. Soft self-consistent pseudopotentials in a generalized eigenvalue formalism. *Phys. Rev. B* **41**, 7892–7895 (1990).

72. Grimme, S. Semiempirical GGA-type density functional constructed with a long-range dispersion correction. *J. Comput. Chem.* **27**, 1788–1799 (2006).

73. Hess, B., Kutzner, C., Van Der Spoel, D. & Lindahl, E. GROMACS 4: Algorithms for highly efficient, load-balanced, and scalable molecular simulation. *J. Chem. Theory Comput.* **4**, 435–447 (2008).

74. Abraham, M. J. et al. Gromacs: high performance molecular simulations through multi-level parallelism from laptops to supercomputers. *SoftwareX* **1–2**, 19–25 (2015).

75. Bell, I. H., Wronski, J., Quoilin, S. & Lemort, V. Pure and pseudo-pure fluid thermophysical property evaluation and the open-source thermophysical property library coolprop. *Ind. Eng. Chem. Res.* **53**, 2498–2508 (2014).

76. Potoff, J. J. & Siepmann, I. J. Vapor-liquid equilibria of mixtures containing Alkanes, Carbon Dioxide, and Nitrogen. *AIChE J.* **47**, 1676–1682 (2001).

77. Jorgensen, W. L. & Tirado-rives, J. The OPLS [Optimized Potentials for Liquid Simulations] potential functions for proteins, energy minimizations for crystals of cyclic peptides and crambin. *J. Am. Chem. Soc.* **110**, 1657–1665 (1988).

78. Cheng, A. & Steele, W. A. Computer simulation of ammonia on graphite. I. Low temperature structure of monolayer and bilayer films. *J. Chem. Phys.* **92**, 3858–3866 (1990).

79. Roux, B. The calculation of the potential of mean force using computer simulations. *Comput. Phys. Commun.* **91**, 275–282 (1995).

80. Souaille, M. & Roux, B. Extension to the weighted histogram analysis method: combining umbrella sampling with free energy calculations. *Comput. Phys. Commun.* **135**, 40–57 (2001).

81. Hub, J. S., De Groot, B. L. & Van Der Spoel, D. G-whams-a free weighted histogram analysis implementation including robust error and autocorrelation estimates. *J. Chem. Theory Comput.* **6**, 3713–3720 (2010).

82. Robeson, L. M. The upper bound revisited. *J. Memb. Sci.* **320**, 390–400 (2008).

Author contributions

L.B. and A.R. contributed equally to this work. K.G.A. and K.V.A. supervised the studies. All authors together conceived the key concepts, discussed the results, and wrote the manuscript.

Competing interests

K.V.A. is a cofounder of a startup looking to commercialize porous graphene membranes for carbon capture. All remaining authors declare no competing interests.

Additional information